Geophysical Journal International

Geophys. J. Int. (2018) **213,** 2096–2111
Advance Access publication 2018 March 22
GJI Geodynamics and tectonics

doi: 10.1093/gji/ggy112

A quantitative approach to the loading rate of seismogenic sources in Italy

Alessandro Caporali,[1] Carla Braitenberg,[2] Paola Montone,[3] Giuliana Rossi,[4] Gianluca Valensise,[3] Alfio Viganò[5] and Joaquin Zurutuza[1]

[1]*Department of Geosciences, University of Padova, 35131 Padova, Italy. E-mail: alessandro.caporali@unipd.it*
[2]*Department of Mathematics and Geosciences, University of Trieste, 34127 Trieste, Italy*
[3]*Istituto Nazionale di Geofisica e Vulcanologia, 00143 Rome, Italy*
[4]*Istituto Nazionale di Oceanografia e Geofisica Sperimentale - OGS, 34010 Trieste, Italy*
[5]*Provincia Autonoma di Trento, Servizio Geologico - 38121Trento, Italy*

Accepted 2018 March 21. Received 2018 February 22; in original form 2017 October 11

SUMMARY

To investigate the transfer of elastic energy between a regional stress field and a set of localized faults, we project the stress rate tensor inferred from the Italian GNSS (Global Navigation Satellite Systems) velocity field onto faults selected from the Database of Individual Seismogenic Sources (DISS 3.2.0). For given Lamé constants and friction coefficient, we compute the loading rate on each fault in terms of the Coulomb failure function (CFF) rate. By varying the strike, dip and rake angles around the nominal DISS values, we also estimate the geometry of planes that are optimally oriented for maximal CFF rate.

Out of 86 Individual Seismogenic Sources (ISSs), all well covered by GNSS data, 78–81 (depending on the assumed friction coefficient) load energy at a rate of 0–4 kPa yr^{-1}. The faults displaying larger CFF rates (4–6 $\pm$ 1 kPa yr^{-1}) are located in the central Apennines and are all characterized by a significant strike-slip component. We also find that the loading rate of 75% of the examined sources is less than 1 kPa yr^{-1} lower than that of optimally oriented faults.

We also analysed 2016 August 24 and October 30 central Apennines earthquakes (M_w 6.0–6.5, respectively). The strike of their causative faults based on seismological and tectonic data and the geodetically inferred strike differ by $<30^\circ$. Some sources exhibit a strike oblique to the direction of maximum strain rate, suggesting that in some instances the present-day stress acts on inherited faults. The choice of the friction coefficient only marginally affects this result.

Key words: Satellite geodesy; Creep and deformation; Rheology and friction of fault zones.

1 INTRODUCTION

Italy is an earthquake-prone country with a long tradition in observational seismology. For many years, the country's unique historical earthquake record has revealed fundamental properties of Italian seismicity and has been used to determine earthquake rates. Palaeoseismological studies conducted in Italy over the past 20 yr have shown that the length of this record – five to eight centuries, depending on areas – is not sufficient to supply a complete record of past seismicity due to characteristic recurrence intervals in the order of 1000–3000 yr (Galli *et al.* 2008; Cowie *et al.* 2017). This circumstance alone may have often led the earthquake potential to be significantly underestimated, and occasionally overestimated (Valensise & Pantosti 2001).

The knowledge of crustal current deformation rates represents a significant boundary condition for modelling seismogenic processes in most of the Italian region, where the typical hypocentral depth is <20 km (Chiarabba & De Gori 2016). A few recent papers have proposed to combine geophysical and geodetic data to infer properties of the crust-mantle coupling (e.g. Palano 2015) and to constrain finite element models where deformation is driven by large-scale processes (e.g. Carafa *et al.* 2015; Carafa & Bird 2016; Carafa *et al.* 2017). Such regional models provide fundamental insight for investigating large-scale geodynamic processes but are too coarse to be used for determining the relative state of stress of adjacent faults.

Over the past two decades, several papers (e.g. King & Cocco 2000; Console *et al.* 2008; Caporali *et al.* 2016, among others) have investigated the Coulomb failure function (CFF) change for specific earthquake sequences which are supposed to be both spatially and temporally correlated. In the CFF approach, a 'receiver' fault changes its state of stress as a consequence of a nearby earthquake.

This method hence reveals whether that fault has been loaded or unloaded by the occurrence of the earthquake. Alternatively, the hypothesis of optimally oriented fault planes was tested using aftershock distributions. The analysis of both background seismicity and aftershock clusters through the principal component analysis (PCA; e.g. Michelini & Bolt 1986; Bressan *et al.* 2016) or through accurate hypocentre locations helps retrieving the preferential planes over which aftershocks distribute (e.g. Valoroso *et al.* 2013; Viganò *et al.* 2015; Meade *et al.* 2017).

GNSS (Global Navigation Satellite Systems) velocities can be translated into observations of interseismic locking and coseismic slip during major earthquakes. This allows the process of stress accumulation and release along major active faults to be monitored in great detail, potentially improving seismic hazard estimates. A notable example is offered by Moreno *et al.* (2010), who used GPS velocities from the decade preceding the 2010, M_w 8.8 Maule (Chile) earthquake to derive a detailed image of the pre-seismically locked Andean subduction zone megathrust. They concluded that the heterogeneity of coseismic slip at the scale of single asperities highlights the potential for future large earthquakes.

In this paper, we focus on the rates of tectonic loading on individual faults (Stein *et al.* 1997; Nalbant *et al.* 2002) as inferred at regional scale from geodetically detected strain as evidence for a source of load on individual faults. In particular, GNSS geodesy provides a 2D plane strain rate that can be converted into an elastic stress rate. The latter can be assumed to approximate the horizontal tectonic loading rate throughout a 15–20-km-thick brittle seismogenic layer. Owing to the dense distribution of Italian geodetic GNSS sites, this stress rate tensor can be calculated for the centroid of several seismogenic sources from v. 3.2.0 of the Italian Database of Individual Seismogenic Sources (DISS database: Basili *et al.* 2008; DISS Working Group 2015). After computing the normal and shear stress rates on the fault plane, the CFF rate is obtained as the difference between the tangential stress rate and the normal stress rate multiplied by an assumed friction coefficient. The obtained CFF rate represents an estimate of the loading/unloading rate of elastic energy on the fault plane. Areas that are historically quiescent but where stress is consistently building up may hence be singled out. In such areas the lack of seismicity may result from creep, or from limited earthquake coupling, or from the incompleteness of the earthquake record, or simply from the fact that the accumulated stress has not yet brought the fault close to rupture.

The paper is organized as follows. We first introduce the tectonic setting and the current knowledge on the present-day stress state of the Italian crust based on independent geophysical data. Then, we review the process of estimating the strain rate eigenvectors from GNSS geodesy; we discuss the interpolation of the CFF rate at the centre of selected ISSs (Individual Seismogenic Sources) and analyse in detail the error budget of the CFF rate, which depends on the uncertainties on the strike, dip and rake angles, on the friction coefficient and on the geodetic data. Finally, we discuss the case of the ISSs that exhibit the smallest and largest CFF rates. We also dwell on the ISSs associated with significant recent earthquakes and show the nearly optimal alignment of their causative faults with the principal axes of the geodetic strain rate tensor.

2 TECTONIC SETTING

The stress field in the lithosphere is generally classified as 1) global scale or first order (wavelength larger than 500 km), ii) regional scale or second order (wavelength between 100 and 500 km) and iii) local scale or third order (wavelength < 100 km) (Heidbach et al., 2010). This latter stress pattern is primarily caused by active faults, but also by the effects of local topography, by the basin geometry, by local intrusions or local density contrasts, by rheological contrasts (e.g. evaporites, overpressured shales, detachment zones), and finally by deglaciation processes (Heidbach *et al.* 2007).

Italy is mostly characterized by third-order scale stress fluctuations, as discussed by Pierdominici & Heidbach (2012), Carafa & Barba (2013) and Montone & Mariucci (2016); in particular, Pierdominici & Heidbach (2012) proposed that in most of the countries the orientation of the principal horizontal stress varies with a rather short wavelength of 150 km or less. This is due to the complexity of plate motions throughout the whole central Mediterranean region; the presence of multiple subduction zones generates highly diverse stress regimes, acting simultaneously and in close geographic proximity, and ultimately causing stress orientations to change on a relatively short wavelength. These active geodynamic processes involve the active fold-and-thrust belts and the Adriatic-Ionian foredeep–foreland systems alike, causing stress regimes to vary from extensional to compressional to strike-slip within short distances.

Montone & Mariucci (2016) and Mariucci & Montone (2018) recently analysed an extended and improved set of Italian stress data, identifying the orientation of the regional stress field and of a number of local stress rotations due to specific tectonic contexts (Fig. 1). Their revised stress map is based on seismicity, deep well breakout and fault observations for the whole Italian territory, together supporting an improved understanding of the current tectonic setting of the Italian region. Fig. 1 shows where most of the stress is concentrated. The main active seismogenic processes are associated with the ∼NE–SW extension observed along the entire Apennines belt, from the northern Apennines of Emilia-Romagna and Tuscany through the Umbria-Marche and Abruzzi regions to the southern Apennines of Campania-Basilicata. A similar deformation pattern is also recognized also by GPS data both in the central and southern Apennines (Devoti *et al.* 2011). In the Calabrian Arc the direction of maximum extension rotates from E–W to WNW–ESE to nearly N–S in the northeastern portion of Sicily, following the arc curvature, and also in this case is accommodated primarily by normal-faulting.

A vigorous compressional tectonic regime characterized mainly by thrust faults is observed only in the external areas of the mountain belts; along the northern Apennines front in the Po Plain and in the northern Adriatic Sea, along the southern margin of the central and eastern Alps and in the Friuli region, in the Ionian Sea along the accretionary wedge of the Calabrian Arc subduction, and offshore in front of the northern Sicily coast (Fig. 1). Also in these cases, the horizontal principal stress orientations mirror the changes in the trend of the related tectonic structures, following each driving tectonic mechanism. In contrast, there is no clear evidence of active compression along the front of the central and southern Apennines (Meletti *et al.* 2000; Montone *et al.* 2012). A well-identified area of ongoing compression defined from concentrated data is found in the eastern external area of the southern Apennines belt up to the Ionian coastline. Here, the dominant regime is strike-slip with ∼NE–SW extension or ∼NW–SE compression orientations over dominantly E–W trending structures.

As briefly mentioned above, in Italy the stress orientations, the trend of tectonic structures and their kinematics vary significantly within a few tens of kilometres. A detailed knowledge of the stress orientations and of their variability along the Italian territory hence comprises a crucial prerequisite for evaluating the strain rates inferred from GNSS velocity data.

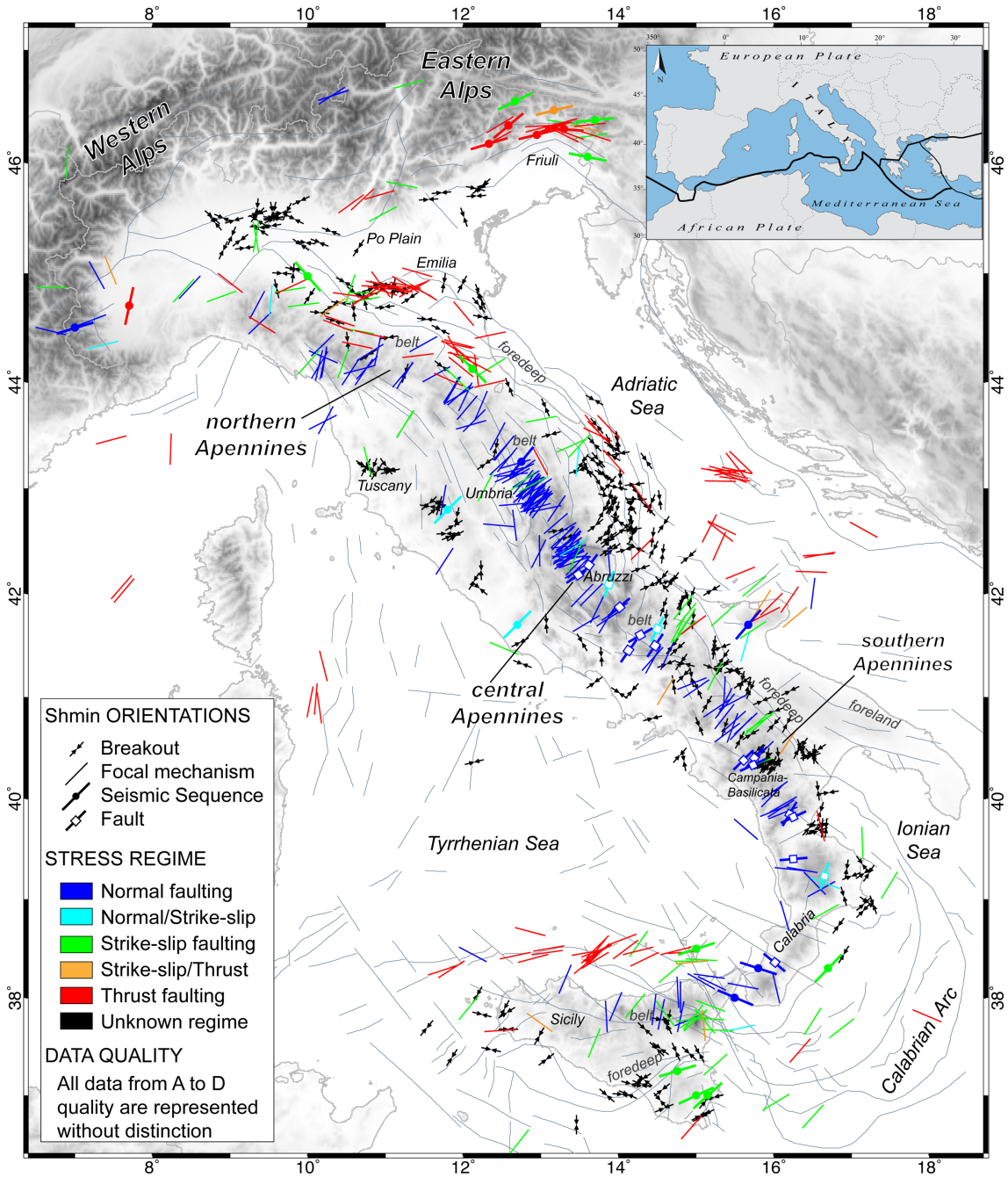

Figure 1. Present-day stress map of Italy, showing the minimum horizontal stress orientation (Shmin) along with the main tectonic features. See text for further information. Modified from Montone & Mariucci (2016).

3 INPUT DATA

3.1 The Database of Individual Seismogenic Sources (DISS)

The Database of Individual Seismogenic Sources (DISS) is a georeferenced repository of tectonic, seismological and palaeoseismological information devoted to applications in the assessment of seismic hazard at regional and national scale (DISS Working Group: http://diss.rm.ingv.it/diss/). The database includes all sources that are deemed capable of generating M_w 5.5 and larger earthquakes. It represents faults in 3D, and its fully parametrized records are ready for automatic processing. The current version of DISS (v. 3.2.0., published in 2015 June) lists 126 Individual Seismogenic Sources (ISS), i.e. faults associated with a specific fixed-size earthquake, and 167 Composite Seismogenic Sources (CSS), i.e. extended crustal faults containing an unspecified number of seismogenic sources that cannot be singled out; for this reason, they are not associated with a specific set of earthquakes or earthquake distribution.

3.2 GNSS velocity data

Over the past two decades the Istituto Nazionale di Geofisica e Vulcanologia (INGV), the Istituto Nazionale di Oceanografia e

Geofisica Sperimentale (OGS), some universities and a few local administrations developed a network that currently includes over 600 permanent GNSS sites spread over the Italian territory. The data are routinely processed according to internationally agreed standards (http://epncb.oma.be/_documentation/guidelines/guidelines_analysis_centres.pdf) to generate velocities in the latest realization of the ITRF frame (IGb08 as of 2017 November). The database of positions and velocities maintained by the University of Padova is regularly updated and provides logsheets, weekly solutions, cumulative solutions (from weekly normal equations stacking), time-series and a discontinuity file with the solution numbers introduced to account for discontinuities in the time-series of each processed site. The velocities of over 500 sites featuring at least 2 yr of continuous tracking and accurately verified time-series are regularly published and updated in the website of Rete GPS Veneto (http://retegnssveneto.cisas.unipd.it). A careful inspection of the the time-series shows the linearity of their behaviour, thus justifying the assumption of a stationary kinematic framework over the past 10–15 yr.

3.3 Seismicity data

INGV also updates and maintains the Catalogo Parametrico dei Terremoti Italiani (CPTI: http://emidius.mi.ingv.it/CPTI/) and the instrumental earthquake database termed *I*talian *S*eismological *I*nstrumental and Parametric *D*ata-bas*E* (ISIDe; http://iside.rm.ingv.it/iside/standard/index.jsp). The CPTI was recently updated to version CPTI15 (Rovida *et al.* 2016), which includes over 4100 earthquakes of M4+ that occurred in the time frame 1000–2014. The CPTI is the basis for Italy's probabilistic seismic hazard assessment and for the associated building codes.

In this work, seismicity data are considered only as input data because they will serve for comparison with the stress rate data obtained for any given ISS. Earthquake data are not used in the calculation of the CFF rate.

4 FROM SCATTERED GNSS VELOCITIES TO STRAIN RATES

We use horizontal velocities and hence concentrate on a 2D, plane strain rate model. To convert the scattered horizontal velocities into strain rate tensors at the centroid of each ISS we need to evaluate a continuous velocity field in the neighbourhood of the centroid of that specific ISS. This procedure requires the availability of as many velocities as needed to compute a reliable horizontal gradient in the neighbourhood of each ISS, where most of the deformation is assumed to take place. The concept of correlation distance for the computation of a strain rate is conveniently embodied into the algorithm of least squares collocation (Caporali *et al.* 2003; Wu *et al.* 2011). This is an autoregressive algorithm where the velocity interpolated at a point P is expressed as a weighted average of the velocities measured at point i ($i = 1 \ldots n$), with a weight function a_{Pi} decreasing with increasing distance from P to the ith GNSS site:

$$v_P = \sum_{i=1}^{n} a_{Pi}\, v_i. \tag{1}$$

For minimum variance, we require that the weight function is computed in terms of the correlation function C_{Pi}:

$$a_{Pi} = \sum_{j=1}^{n} C_{Pj}\, C_{ij}^{-1}, \tag{2}$$

where C_{ij} is the correlation between the measured velocities as a function of their relative distance (see Appendix A). By construction, whenever the point P coincides with one of the data-points (a GNSS site in our case), the least squares algorithm returns exactly the input value. Conversely, the measured velocities are affected by an uncertainty and by mutual correlation, both described by the variance–covariance matrix w_{ij} resulting from the stacking of the multiyear normal equation. For this reason, and in order to low-pass filter spurious velocities which may be affected by local disturbances, it is convenient to modify the covariance function in eq. (2) as follows:

$$C_{ij} \rightarrow C_{ij} + w_{ij} \tag{3}$$

Eq. (3) enables low-pass filtering of spurious velocity measurements, for example resulting from monument instabilities. Scaling the matrix w provides additional smoothing that may be useful to isolate the medium/long wavelength of the regional velocity field. In general, the smoother the velocity field, the smaller the strain rate, the lower the spatial resolution of the dense velocity field. Our smoothing factor was selected to remove the velocity outliers (3σ criterion).

The correlation function must have unity value and zero derivative at the origin. As a first approximation one can consider an isotropic correlation function depending on a correlation distance d_0:

$$C_{Pi} = \frac{1}{1 + \left(\frac{d_{Pi}}{d_0}\right)^2}, \tag{4}$$

where d_{pi} is the distance between the ith GNSS site and the computation point P. The horizontal gradient of the velocity at P follows from differentiation in the North and East directions of eq. (1) (see Appendix A). The 2D strain rate is the symmetrical part of the velocity gradient tensor. The eigenvalues and eigenvectors of the strain rate tensor are computed by matrix diagonalization, yielding a maximum/minimum strain rate (typically the most extensional/compressional, corresponding to a positive/negative horizontal derivative of the velocity field) and the azimuth ϑ of the most extensional strain rate. Details are given in Caporali *et al.* (2003; eqs 1–5).

Assuming that the coverage of GNSS velocities in a neighbourhood (typically at least 50 km) of the studied site (normally the centroid of the ISS) is sufficiently dense, the value of the correlation distance d_0 must be constrained by the velocity data themselves. We compute one d_0 for each ISS by analysing the correlation profile of the local GNSS site velocities. More precisely, for each ISS we compute the shear strain rate (the absolute value of the difference between the two eigenvalues) for increasing values of the correlation distance, i.e. for an increasing number of GNSS sites, to find the value of d_0 that maximizes the shear strain rate (Fig. 2). Longer d_0 distances tend to include uncorrelated velocities, hence reducing the estimate of the shear strain rate. The value of d_0 which maximizes the shear strain rate ensures that all the correlated velocities contribute to the computation of the strain rate tensor. As expected, we find correlation distances between 40 and 100 km for the different ISSs (Table 1). For 40 out of 126 ISSs, we did not compute the strain rate, as they fall in one or more of the following exclusion criteria: (a) insufficient population of GNSS velocities (less than 4) within the search range; (b) unclear behaviour of the shear strain rate as a function of d_0; (c) the retrieved stress regime is inconsistent with the geologic evidence reported in the DISS. By 'unclear behaviour' we refer to the cases where faults with different strikes coexist in the

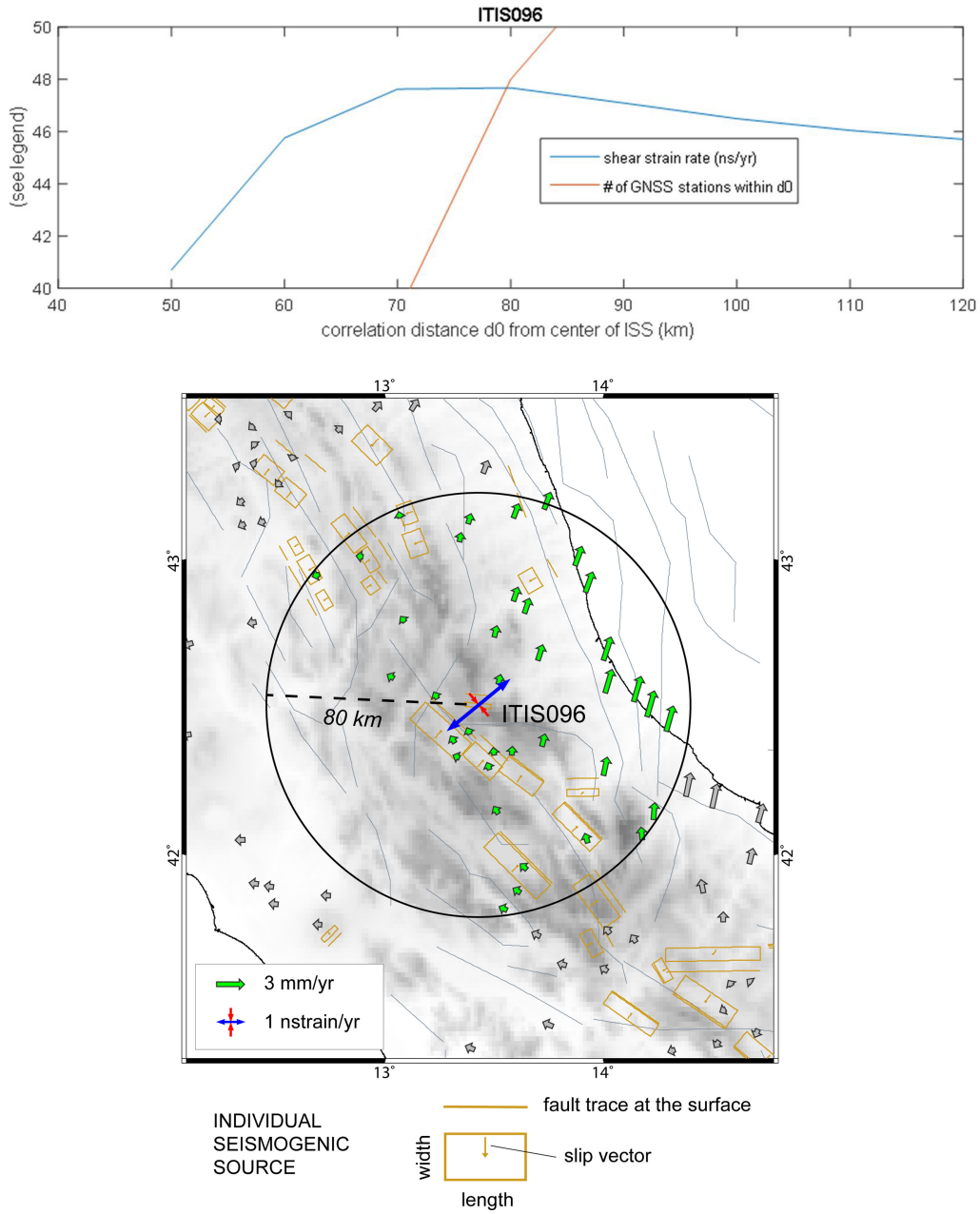

Figure 2. (Top) Dependence of the shear strain rate on the scale distance d_0 used in the correlation function for the ITIS096 Individual Seismogenic Source: the maximum shear strain rate is achieved at a distance of 80 km from the centroid of the ISS with 48 GNSS sites lying within that distance. The plot suggests that including the contribution of more sites (i.e. increasing d_0) with uncorrelated shear strain rate does not change the shear strain rate significantly. (Bottom) Distribution of the GNSS sites (green arrows) within ca. 80 km from the centroid of ITIS096 (solid circle). Some velocities are too small to be shown, or overlap near sites. Extension is shown in blue, compression in red.

same area. In these cases, the GNSS velocities – and their gradients – reflect the sum of the movement generated by close sources with different strikes. Consequently, it is impossible to obtain strain rates pertaining uniquely to one fault. By 'inconsistent stress regime' we mean that the largest stress rate eigenvector is opposite to the horizontal projection of the slip vector of the fault. This condition is generally associated with a poor geometry of the neighbouring GNSS sites, even if their number is sufficient (>4). An example of case (c), where the geodetic data and the geologic data appear to disagree, is given by ITIS140 (Veronese). A discussion of this case is deferred to Section 8.3. All ISSs that were found uncompliant with at least one of criteria (a), (b) and (c) mentioned above have hence been discarded as not sufficiently constrained by the currently available GNSS data.

The last two entries in Table 1 refer to seismogenic sources that are not currently listed in the DISS database: they correspond to the causative faults of the 2016 August 24, M_w 6.0 Amatrice and of the 2016 October 30 Norcia earthquakes, respectively. Their fault plane solutions are well known and they will be included in the next release of the DISS.

Fig. 3 shows the velocities (ETRF2000 frame) of the GNSS sites and the eigenvectors of the strain rate interpolated at the centre of each well-constrained ISS.

Table 1. List of 86 Individual Seismogenic Sources (out of 126 currently listed in the current release DISS 3.2.0 database) selected for this study as properly illuminated by GNSS data. For each ISS, we supply the coordinates of the centroid, the name and description as in the DISS database, plus the strike, dip and rake angles, which are input values for our analysis. We then provide the correlation distance d_0 and the number of GNSS sites within d_0 from the ISS centroid, which most contributed in the computation of the eigenvectors of the strain rate tensor. We then list the CFF rate (yr^{-1}) for a friction coefficient of 0.5, and the optimal rate of CFF obtained by varying the three orientation angles until the CFF rate reaches a maximum. A nominal friction of 0.5 is assumed. The values of the optimal angles are supplied for each analysed ISS in the Additional Material of Supporting Information as datasheets in Google Earth format. The last two entries (Amatrice and Norcia) are not listed in the DISS 3.2.0 and correspond to the M_w 6.0 and 6.5 earthquakes that occurred, respectively, on 2016 August 24 and October 30, and that we used as a test: in both cases the SW-dipping plane is assumed to be the actual rupture plane. Uncertainties in the angles and in the CFF rate estimates are discussed in text.

Lon (°E)	Lat (°N)	Source ID	Source name	Strike (°)	Dip (°)	Rake (°)	d_0 (km)	Data points	CFF (kPa yr^{-1}), $\mu_f = 0.5$	CFF (kPa yr^{-1}), $\mu_f = 0.5$ and optimally oriented fault
13.61	41.96	ITIS002	Fucino Basin	135	60	270	50	24	2.38	3.57
13.97	41.84	ITIS003	Aremogna-Cinque Miglia	144	50	270	100	72	1.02	1.7
14.47	41.50	ITIS004	Boiano Basin	304	55	270	50	23	2.64	3.9
14.74	41.29	ITIS005	Tammaro Basin	311	60	270	50	25	1.51	2.33
15.10	41.07	ITIS006	Ufita Valley	275	64	237	90	61	0.57	1.43
15.78	40.35	ITIS008	Agri Valley	316	60	270	50	24	1.63	2.1
15.60	40.53	ITIS010	Melandro-Pergola	317	60	270	50	26	2.87	4.83
16.02	38.34	ITIS012	Gioia Tauro Plain	30	30	270	50	8	−0.43	1.32
15.60	38.05	ITIS013	Messina Straits	30	29	270	50	6	0.03	1.55
12.96	37.79	ITIS014	Belice	277	55	127	100	13	0.3	0.71
12.84	43.09	ITIS017	Colfiorito North	143	40	275	90	59	−0.03	1.12
12.93	43.00	ITIS018	Colfiorito South	148	40	277	90	61	0.01	1.15
12.93	42.91	ITIS019	Sellano	144	40	260	90	64	0.26	1.13
15.97	41.72	ITIS020	Monte Sant'Angelo	280	80	215	50	7	−0.67	1.03
13.10	43.75	ITIS024	Mondolfo	122	30	90	50	13	−0.66	2.16
13.88	42.09	ITIS027	Sulmona Basin	135	60	270	50	25	3.75	5.28
13.95	41.70	ITIS028	Barrea	152	50	264	50	21	−0.31	0.59
13.70	43.59	ITIS029	Conero offshore	145	40	90	50	8	0.1	1.04
13.26	43.64	ITIS030	Senigallia	142	30	90	50	11	−0.16	1.93
12.94	43.84	ITIS031	Fano Ardizio	132	30	90	50	13	−0.24	1.54
12.81	43.92	ITIS032	Pesaro San Bartolo	110	35	90	110	50	−0.68	0.41
12.74	44.04	ITIS033	Rimini offshore South	132	30	90	120	58	−0.27	0.68
12.66	44.09	ITIS034	Rimini offshore North	132	30	90	100	44	−0.1	0.75
12.52	44.00	ITIS035	Rimini	132	30	90	70	24	−0.08	1.22
12.46	44.10	ITIS036	Val Marecchia	132	30	90	80	30	−0.09	1.17
15.05	38.26	ITIS045	Patti Gulf	147	83	180	50	7	−0.02	0.16
12.94	43.38	ITIS048	Fabriano	135	20	90	50	25	−0.38	1.98
13.10	43.16	ITIS049	Camerino	160	20	90	50	18	−0.05	2.31
10.32	44.18	ITIS050	Garfagnana North	305	40	270	120	55	−0.05	0.32
10.52	44.07	ITIS051	Garfagnana South	307	40	270	50	14	0.28	0.71
14.94	41.69	ITIS052	San Giuliano di Puglia	267	82	203	50	20	3.22	4.57
14.81	41.70	ITIS053	Ripabottoni	261	86	195	50	22	3.94	5.12
15.35	41.71	ITIS054	San Severo	266	80	215	70	30	−0.49	1.09
13.14	43.05	ITIS055	Sarnano	160	20	90	50	18	0.09	1.98
13.71	38.37	ITIS056	Southern Tyrrhenian	251	53	112	60	5	0.06	0.67
12.75	41.73	ITIS059	Velletri	225	70	270	50	16	−0.1	0.6
12.59	43.04	ITIS060	Bastia	330	30	270	100	69	0.52	0.66
12.66	42.97	ITIS061	Foligno	330	30	270	100	72	0.46	0.64
12.72	42.86	ITIS062	Trevi	330	30	270	120	95	0.67	0.84
12.18	43.48	ITIS063	Monterchi	315	30	270	50	23	1.66	2.97
12.22	43.51	ITIS065	Selci Lama	130	45	270	50	24	2.67	3.69
10.49	43.52	ITIS066	Orciano Pisano	337	50	270	120	46	0.11	0.42
10.03	44.22	ITIS067	Aulla	320	40	270	120	52	−0.35	0.09
07.26	44.84	ITIS071	Torre Pellice	62	45	135	150	47	−0.14	0.12
07.36	44.87	ITIS073	Pinerolo	76	45	150	110	35	−0.13	0.28
15.01	37.15	ITIS074	Monte Lauro	57	45	70	60	10	0.81	1.2
15.48	40.68	ITIS078	San Gregorio Magno	300	60	270	120	86	1.73	2.22
15.80	41.29	ITIS080	Cerignola	269	80	180	130	92	0.81	1.86
15.66	40.98	ITIS081	Melfi	269	80	180	50	18	2.52	5.18
15.52	41.29	ITIS082	Ascoli Satriano	269	80	180	50	16	3.63	5.77
16.37	41.28	ITIS083	Bisceglie	269	80	180	50	10	0.46	0.96
15.85	40.68	ITIS084	Potenza	95	88	175	50	21	2.87	5.23
09.91	44.37	ITIS085	Pontremoli	329	42	270	50	13	−0.46	0.3
15.46	41.03	ITIS088	Bisaccia	280	64	237	50	20	3.32	5.24
14.28	41.60	ITIS089	Carpino - Le Piane	330	60	270	50	22	0.19	0.78
11.50	44.89	ITIS090	Ferrara	88	50	90	50	13	1.39	1.67

Table 1. Continued

Lon (°E)	Lat (°N)	Source ID	Source name	Strike (°)	Dip (°)	Rake (°)	d_0 (km)	Data points	CFF (kPa yr^{-1}), $\mu_f = 0.5$	CFF (kPa yr^{-1}), $\mu_f = 0.5$ and optimally oriented fault
15.06	41.24	ITIS092	Ariano Irpino	277	70	230	50	24	1.12	3.1
13.91	42.21	ITIS094	Tocco da Casauria	89	70	230	50	25	5.14	6.04
14.50	41.66	ITIS095	Frosolone	269	70	230	50	24	2.13	2.83
13.43	42.51	ITIS096	Isola del Gran Sasso	95	75	225	80	48	2.08	2.63
16.25	39.44	ITIS097	Luzzi	180	65	270	50	10	−0.11	1.57
16.26	39.35	ITIS098	Castiglione Cosentino	180	60	270	50	10	0.32	2.05
12.15	45.86	ITIS101	Montello	242	40	80	50	30	0.13	0.4
11.87	45.82	ITIS102	Bassano-Cornuda	240	35	80	50	32	0.44	0.81
15.07	37.54	ITIS106	Gravina di Catania	246	30	90	50	7	−0.45	2.28
11.07	44.85	ITIS107	Mirandola	108	30	90	50	12	2.04	2.37
12.70	46.21	ITIS108	Maniago	237	30	90	50	26	1	1.52
12.86	46.20	ITIS109	Sequals	254	40	90	50	26	1.19	1.25
12.80	46.29	ITIS112	Tramonti	268	35	90	50	22	1	1.27
11.83	45.82	ITIS113	Monte Grappa	60	35	80	50	34	0.51	0.81
13.26	46.24	ITIS119	Tarcento	277	30	90	50	17	1.1	1.11
13.14	46.25	ITIS120	Gemona South	290	30	105	60	26	0.9	0.96
12.43	46.03	ITIS124	Cansiglio	214	50	60	50	28	0.52	1.23
12.55	46.12	ITIS125	Polcenigo-Montereale	220	40	80	50	31	1.04	1.57
13.38	45.97	ITIS126	Medea	285	45	120	60	20	0.37	0.62
11.62	45.75	ITIS127	Thiene-Bassano	244	30	80	50	31	0.36	0.38
08.28	43.88	ITIS130	Imperia Promontory	240	30	90	50	5	0.13	0.24
13.45	42.32	ITIS131	Paganica	133	43	275	80	48	0.44	1.91
16.37	41.65	ITIS133	Gondola West	278	85	225	90	19	−0.94	0.21
11.32	44.85	ITIS134	Finale Emilia	115	43	90	50	12	1.69	2.11
10.33	44.55	ITIS135	Neviano degli Arduini	98	55	79	50	12	0.06	0.65
14.13	41.45	ITIS138	Aquae Iuliae	125	65	270	50	21	1.41	2.23
16.19	38.80	ITIS139	Sant'Eufemia	31	38	270	50	10	0.43	1.15
10.99	45.27	ITIS140	Veronese	248	40	90	50	20	−0.29	0.73
13.89	46.08	SIIS001	Idrija	310	80	176	50	10	0.38	0.68
13.66	46.30	SIIS002	Bovec-Krn	315	82	171	50	13	0.41	0.7
13.20	*42.75*	*EQ 240 816*	*Amatrice*	*157*	*43*	*284*	*140*	*111*	*0.76*	*1.75*
13.11	*42.84*	*EQ 301 016*	*Norcia*	*151*	*47*	*271*	*50*	*19*	*0.45*	*1.82*

5 COMPUTING THE CFF RATE

To compute the CFF rate at the centroid of each ISS, we first need to convert the horizontal strain rate (ε) into a stress rate (σ). We assume that the upper crust, which completely includes the seismogenic layer for the considered case study, has an elastic rheology (cf. discussion in Burov 2010). The stress rate is defined in terms of the Lamé constants Λ and μ by Hooke's law:

$$\sigma_{ij} = \Lambda\,(\varepsilon_{\mathrm{NN}} + \varepsilon_{\mathrm{EE}})\,\delta_{ij} + 2\mu\varepsilon_{ij}\; i, j = \mathrm{E, N, U}, \tag{5}$$

where E, N, U denote the east, north and up directions, respectively, and δ_{ij} is the Kronecker delta. Note that the plane strain rate assumption implies $\varepsilon_{iU} = 0$: yet $\sigma_{UU} \neq 0$. We assume that the stress rate obtained from eq. (5) and defined in terms of strain rates measured at the surface remains constant across the full depth of the seismogenic layer, typically 10–20 km. Then we compute the normal σ_{n} and shear τ projections of the stress rate tensor at the centroid of each ISS, given its strike, dip and rake angles as listed in the DISS.

The CFF rate is eventually computed, given a friction coefficient μ_{f}:

$$\mathrm{CFF} = \tau + \mu_{\mathrm{f}}\sigma_n. \tag{6}$$

To do this, we use the strike (α), dip (δ) and rake (λ) supplied in DISS for each ISS to construct the normal $\boldsymbol{n}$ and slip $\boldsymbol{d}$ versors in the (north, east, up) local frame:

$$\begin{aligned} d &= \begin{pmatrix} \sin\alpha & -\cos\alpha & 0 \\ \cos\alpha & \sin\alpha & 0 \\ 0 & 0 & 1 \end{pmatrix} \begin{pmatrix} 1 & 0 & 0 \\ 0 & \cos\delta & -\sin\delta \\ 0 & \sin\delta & \cos\delta \end{pmatrix} \begin{pmatrix} \cos\lambda \\ \sin\lambda \\ 0 \end{pmatrix} \\ n &= \begin{pmatrix} \sin\alpha & -\cos\alpha & 0 \\ \cos\alpha & \sin\alpha & 0 \\ 0 & 0 & 1 \end{pmatrix} \begin{pmatrix} 0 \\ -\sin\delta \\ \cos\delta \end{pmatrix}. \end{aligned} \tag{7}$$

Finally, the normal and shear stresses are computed (repeated indexes imply summation):

$$\tau = \sigma_{ij}\, n_i d_j;\;\; \sigma_n = \sigma_{ij}\, n_i n_j. \tag{8}$$

For the computation of eq. (6), we use the subroutine calc_coulomb.m of the software Coulomb 3.3 (Lin & Stein 2004; Toda *et al.* 2005). Details on the computation of the CFF are given in Appendix B.

The selection of the friction coefficient requires considerable attention. The friction coefficient weights the contribution of the normal stress rate to the CFF rate, so that the sign of the CFF rate depends on the friction coefficient. A reasonable range for the friction coefficient is 0.2–0.8 (e.g. Rivera & Kanamori 2002, Smith & Faulkner 2010 and references therein). Because there is no *a priori* constraint on the value of the friction coefficient, we computed the CFF rate under two alternative hypotheses: (a) the average friction coefficient μ_{f} is set to 0.5 for all the ISSs; (b) μ_{f} is estimated from the fault geometry, under the assumption that the

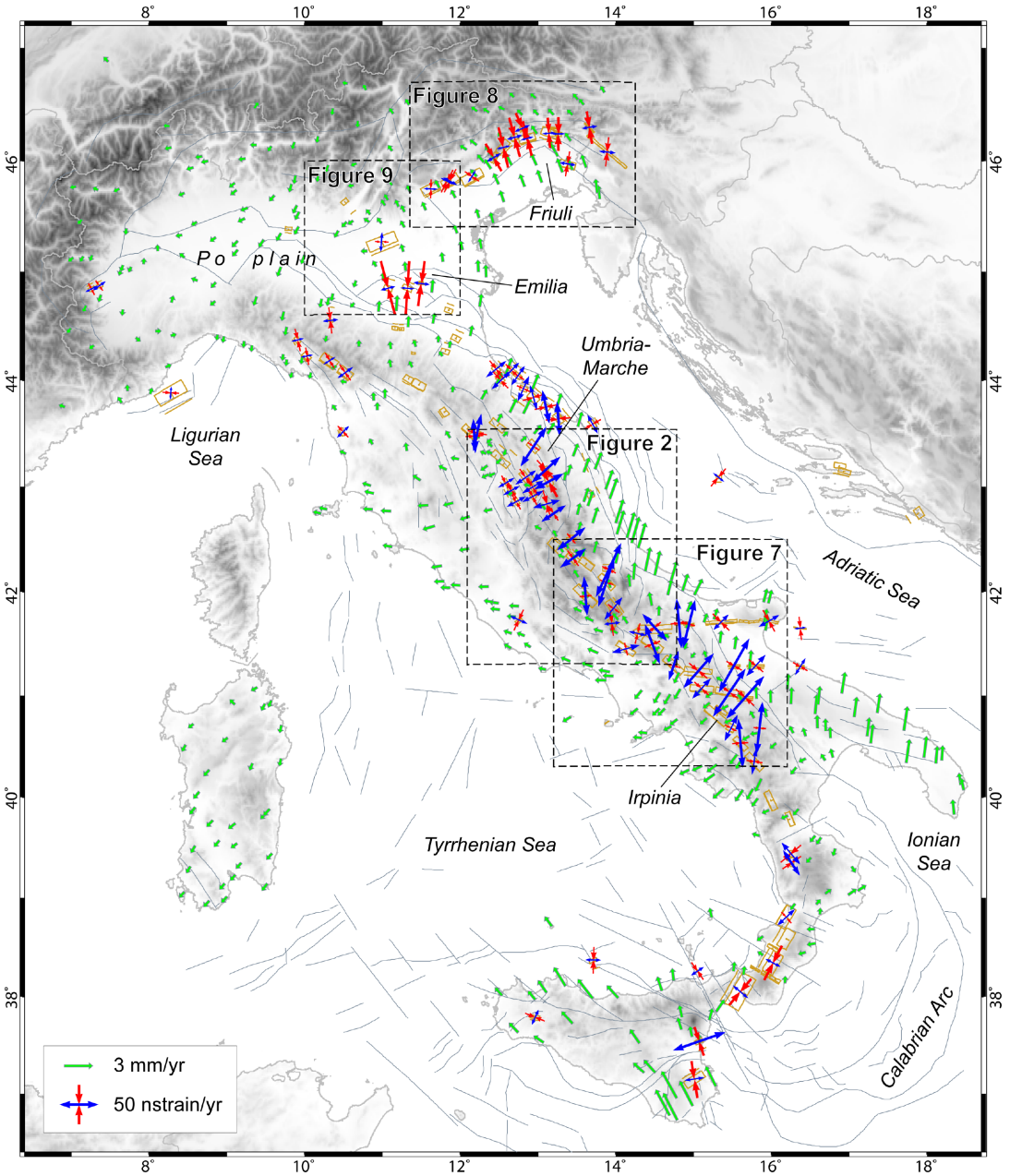

Figure 3. Eigenvectors of the strain rate tensor inferred from GNSS velocities (green arrows) are interpolated to the centre of each of the 86 ISSs (Individual Seismogenic Sources from the DISS 3.2.0 Data Base: brown rectangles) that were selected as sufficiently illuminated by GNSS data. Extension is shown in blue and compression in red. Major tectonic lineaments are shown in grey.

ISSs are oriented so that the CFF rate is maximal (see Appendix B and Anderson 1951):

$$\mu_f = \frac{\sin\lambda}{\tan 2\delta}, \tag{9}$$

where λ and δ are the rake and dip angles of each ISS.

It should be stressed that the value of the friction coefficient computed with eq. (9) does not apply to strike-slip faults with vertical or near vertical dip such as ITIS045, ITIS052 and ITIS053. Neverthless, we have done the computation also for these faults in order to test the dependence of the CFF rate on the assumed value of the friction coefficient.

6 ERROR BUDGET OF THE CFF RATE

To test our approach, we first take $\lambda = \mu = 30$ GPa, corresponding to a Young modulus of 75 MPa and a Poisson ratio of 0.25, which is adequate for most sedimentary and metamorphic rocks (Turcotte & Schubert 2014). We emphasize that these are nominal values that are only acceptable in a test phase: we will need to assign better-calibrated values to each ISS, for example using constraints from the v_p/v_s ratio. We also need to set a sensitivity scale of our data. Our input data are GNSS velocities, for which a conservative uncertainty estimate is 0.2 mm yr^{-1} on account of both white and coloured noise (Caporali 2003). For the computation of strain rates, we require that at least four GNSS sites fall within a 50 km radius from the centroid of any given ISS. Consequently, if the uncertainties in the velocities

are statistically independent, as a rule of thumb we may expect the uncertainty on the strain rate to be in the order of (4 (0.2/50 10^6)^2)$^{1/2} \sim 8$ nstrain yr^{-1}. The average strain rate of the studied ISSs is about 60 nstrain yr^{-1}. To be conservative, we divide this figure by a factor of two and assume (8/30) radians or 16° as a typical uncertainty in the orientation of the principal stress rate, which is comparable with the uncertainties of the stress field obtained from geophysical and seismological data (Montone & Mariucci 2016). More detailed calculations based on error propagation through the computational chain confirm these order-of-magnitude estimates (Mastrolembo Ventura & Caporali 2017).

As for the CFF rate, the contribution of the friction coefficient to the total uncertainty is relatively modest and can be estimated as follows. Because the average normal stress rate is 0.3 kPa yr^{-1} (Table 1), and assuming nominally $\mu_f = 0.5$, a 50% increase in the friction coefficient will change the CFF rate by (0.3 0.5 0.5) $\sim$ 0.1 kPa yr^{-1}. Consequently, the uncertainty in the strain rate due to uncertainties in the velocities and the friction coefficient maps into a stress rate uncertainty of roughly 0.3–0.5 kPa yr^{-1}. We conclude that an order-of-magnitude estimate of the uncertainty of the CFF rate resulting from uncertainties in the GNSS velocities and in the friction coefficient can be conservatively taken equal to 0.5 kPa yr^{-1}. Fig. 4 compares the CFF calculation for different choices of the friction coefficient: a fixed 0.5 for each ISS and a variable value, according to eq. (9). Figs 4(a) and (b) are very similar, supporting the idea that the results are not significantly affected by the assumed value of the friction coefficient, as discussed in more detail in Section 7.

The largest contribution to the error budget of the CFF rate comes from the strike, dip and rake angles assigned to each ISS in the DISS. These angles refer to an idealized condition of uniform slip on a rectangular fault. Uncertainties are normally unavailable, but we can estimate that 20°–30° is a conservative value for class C Sh_{min} data. Two questions should then be posed: (a) how much our estimates of the CFF rate will change if we vary the reference angles (strike, dip, rake) by an amount comparable with their nominal uncertainty? and (b) can 'optimal' angles – i.e. angles which maximize the CFF rate – be significantly different from fault plane angles for individual faults in the DISS?

To address the question (a) we computed the value of the CFF rate for a 20° change in each of the strike, dip and rake angles, and found that the root sum squared is typically 10% of the nominal value, assuming a fixed friction coefficient of 0.5. Knowing that the uncertainty in the strain rate and friction coefficient contributes with typically 0.5 kPa yr^{-1} and that the maximum CFF rate is 5 kPa yr^{-1}, we conclude that the overall uncertainty in the values of the CFF rate, on account of uncertainties in the strain rate, friction coefficient and fault angles, should be 0.8 kPa yr^{-1} or less. We therefore take 1 kPa yr^{-1} as a conservative estimate of the global error budget on the CFF rate.

To address question (b), we varied the strike, dip and rake angles in the range ±45°, ±15° and ±90°, respectively, relative to the nominal values listed in the DISS, for a fixed friction coefficient of 0.5, and identified the combination which maximizes the CFF rate. We summarize our findings in Fig. 5 and Table 1 (last column). Fig. 5 shows that for the majority of the analysed ISSs, the CFF rate computed with the nominal strike/dip/rake angles differs by less than 1 kPa yr^{-1} relative to its largest value. We therefore conclude that the majority of the analysed ISSs are optimally oriented.

7 DISCUSSION

We first examine the effect of choosing two different approaches for establishing the friction coefficient. Fig. 4 compares the statistical distributions of the CFF rate for fixed (top) and variable (bottom) friction coefficient. Recall that by variable friction coefficient we mean that μ_f was computed using eq. (9) based on the angles provided by DISS for each ISS.

Fig. 4 (bottom) shows that if we assume a friction coefficient optimized for the dip and rake of a fault (eq. 9) the CFF rate increases by up to 1 kPa yr^{-1}. All faults for which we computed the CFF rate are displayed with colour-coding in Fig. 6. Figs 4 and 5 further indicate that the majority of the examined faults are positively coupled with the regional field at the relatively modest rate of less than 5 kPa yr^{-1}, with a few notable exceptions located in Central Italy. Table 1 shows that these are ITIS052 (San Giuliano di Puglia), ITIS053 (Ripabottoni), for which we find a loading rate of 3.22 and 3.94 kPa yr^{-1}, respectively, and ITIS094 (Tocco da Casauria) with 5.14 kPa yr^{-1}. By comparison, Stein *et al.* (1997) consider for the North Anatolian Fault an average secular stressing rate of 15 kPa yr^{-1}, whereas Nalbant *et al.* (2002) reported a much lower estimate of 5.6 kPa yr^{-1} for the East Anatolian Fault. For Italy, independent estimates of shear stress rate in the Apennines (Catalli *et al.* 2008) and in the Po Plain-Adriatic front in Northern Italy (Dahm *et al.* 2015) are both 0.7 kPa yr^{-1}. This figure is not significantly different from our independent estimates. For the Alto Tiberina fault, Anderlini *et al.* (2016) report 2 kPa yr^{-1} for the CFF rate, which is very close (the difference is $<$ 1 kPa yr^{-1}) to our estimates for the ITIS065 Selci Lama, which falls within the Alto Tiberina fault system (see Table 1).

7.1 Sources displaying the largest positive and negative CFF rates

Fig. 7 shows the ISSs that exhibit a CFF rate larger than 3 kPa yr^{-1}. This value was arbitrarily chosen to highlight faults with maximal loading. ITIS052 and ITIS053 are, respectively, associated with the 2002 October 31 and November 1, M_w 5.7 and 5.8 San Giuliano di Puglia earthquakes, which were caused by pure right-lateral strike-slip at a depth of 16–20 km. It is remarkable that Di Luccio *et al.* (2005) estimate that the minimum principal stress (i.e. the most extensional stress) is elongated in the ∼N–S direction, which agrees well with the geodetic estimates of the strain rate eigenvectors shown in Fig. 3: the extensional strain rate has an azimuth of only 14°, and the compressional strain rate is negligibly small. We conclude that for these two seismogenic sources a regional extensional stress is accommodated by strike-slip seismicity as already confirmed by Di Bucci & Mazzoli (2003), Valensise *et al.* (2004), Vallée & Di Luccio (2005) and Chiarabba *et al.* (2005). Additional examples of suboptimal alignment of the regional stress to fault orientations will be discussed in the next section.

Central Italy has the maximum loading rate. Empty squares indicate the epicentres of historical earthquakes taken from the CPTI2015 catalogue (Rovida *et al.* 2016).

In the DISS database, the ITIS094 (Tocco da Casauria) is held responsible for the 1456 December 5–30 earthquake sequence, reportedly the largest and most destructive event to have ever occurred in the Italian peninsula. The CPTI15 catalogue assigns M_w 7.2 to the full earthquakes sequence, implicitly collapsing all the largest events into a single mainshock. In contrast, Fracassi & Valensise (2007) proposed that the 1456 sequence be in fact composed by various sub-events, but also maintain that only three main events

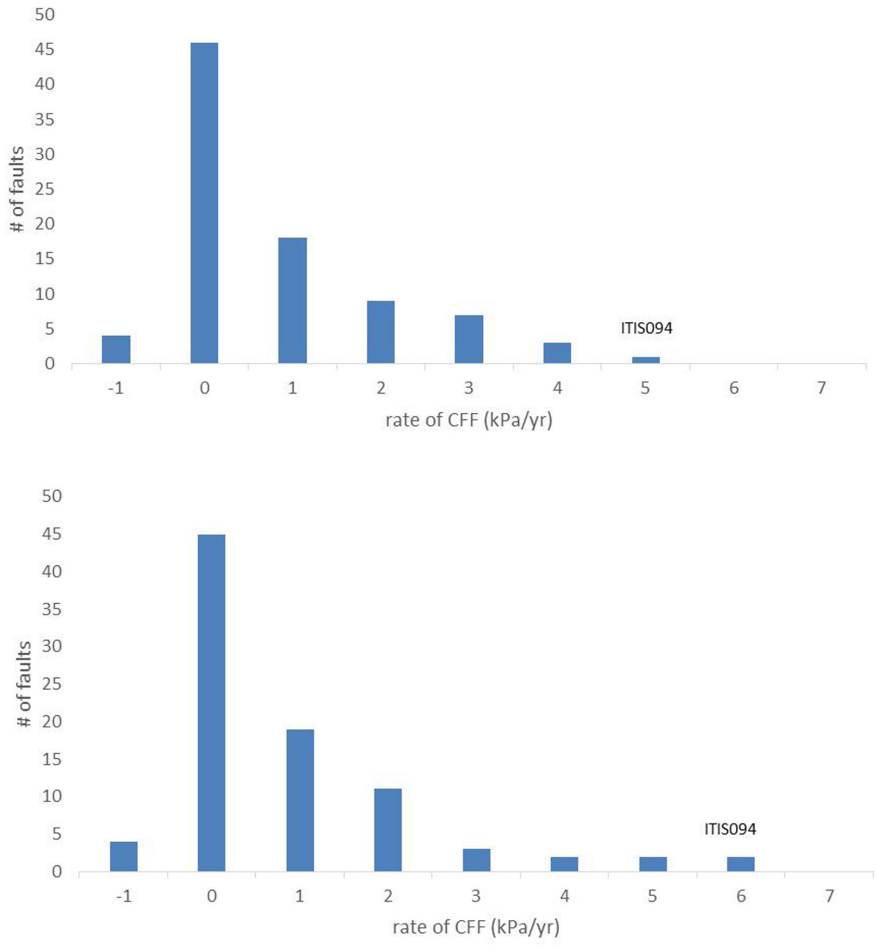

Figure 4. Statistical distribution of the ISSs according to the CFF rate for a fixed (μ_f= 0.5; top) and variable (bottom) friction coefficient, computed using eq. (9).

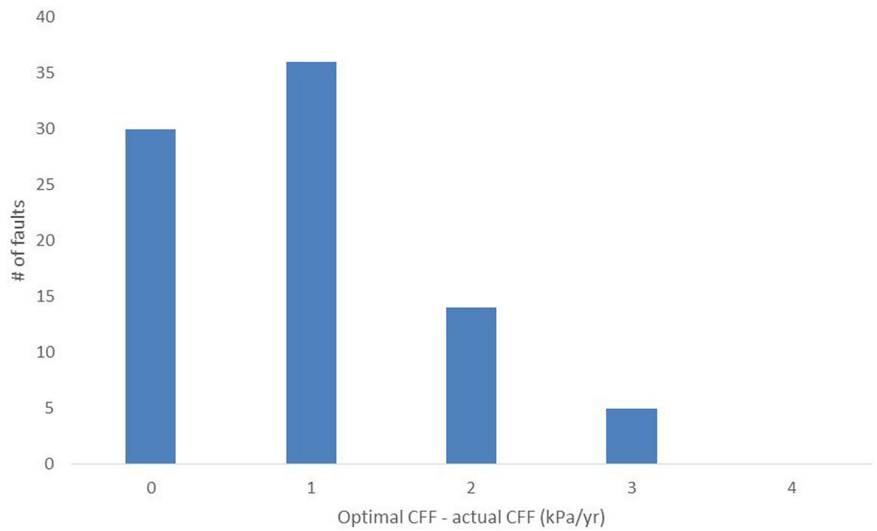

Figure 5. Statistics of the orientation of the ISSs relative to optimally oriented planes. The bin size is calibrated on an estimated uncertainty of CFF rate values equal to 1 kPa yr^{-1}.

occurring between 1456 December 5 and 30 are responsible for most of the damage. According to these investigators, the tectonic environment responsible for these earthquakes falls in between the dominantly extensional domain running along the Apennines axis and the mainly right-lateral strike-slip domain characterizing the Apulian foreland.

It is legitimate to conclude that the seismic provinces showing the highest CFF rates have also been affected by significant

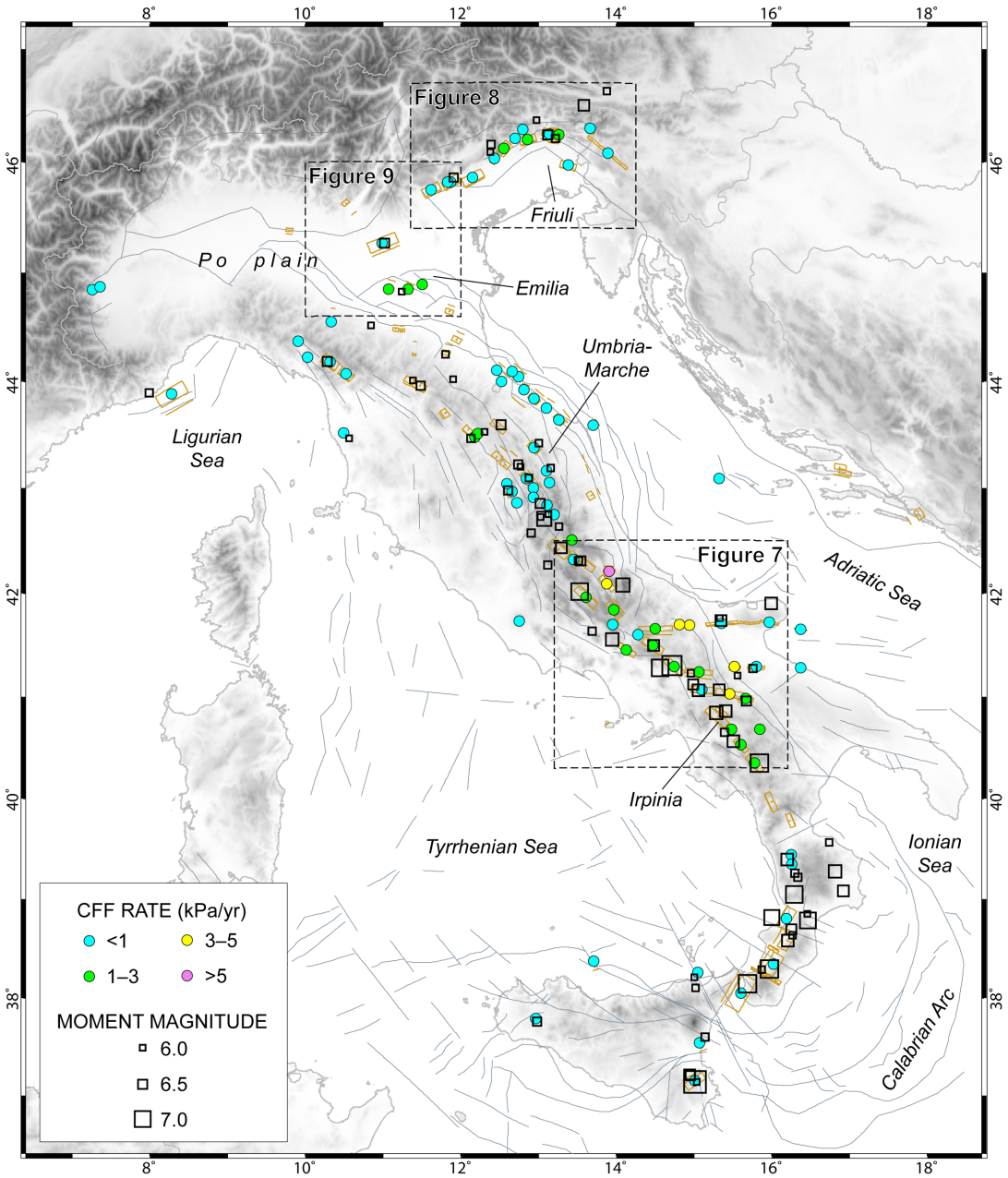

Figure 6. Classification of the selected ISSs according to their CFF rate (constant friction $\mu_f = 0.5$) and largest earthquakes from the CPTI15 catalogue (Rovida *et al.* 2016), shown by empty squares.

earthquakes. Neverthless, regions that hosted large historical earthquakes appear to be characterized by a low CFF rate. Comparing the results shown in Table 1 with the maximum expected magnitude reported in DISS for each ISS one may conclude that there exist ISSs with low (<3 kPa yr^{-1}) CFF which are associated with M_w 7.0+ earthquakes (e.g. ITIS002, ITIS005, ITIS010, ITIS013, ITIS074). Unfortunately, no CFF rate information is available for the Calabrian arc, the most active portion of the Italian peninsula, essentially due to the insufficient number of GNSS sites. Negative CFF rates near the threshold of −1 kPa yr^{-1} are found for ITIS133 (Gondola West) for fixed and variable friction (Table 1).

7.2 Alignment of the fault strike to the orientation of the geodetic strain rate field

A misalignment between the strike of a fault and the maximum eigenvector of the strain rate tensor is often an indication that seismogenic slip occurs on inherited faults, i.e. older faults which have been reactivated with a different stress regime. An example of this circumstance is given by the seismogenic sources of Friuli, as discussed by Viganò *et al.* (2013; 2015), Bressan *et al.* (2016), and Restivo *et al.* (2016). As shown in Fig. 8, in northeastern Italy the strike of the main faults is nearly perpendicular to the most compressive horizontal principal stress only near the tip of the Adriatic indenter (Massironi *et al.* 2006; Robl *et al.* 2017) where the Gemona ISS (ITIS120) is located. To the east, the compressional eigenvector

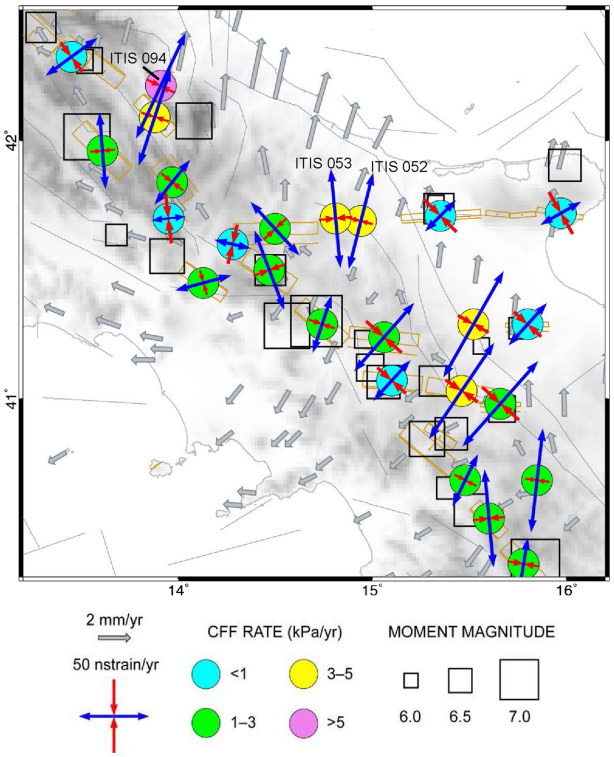

Figure 7. The ISSs in central-southern Italy are plotted along with their CFF rate (constant friction), measured GNSS velocities (grey vectors) and surface strain rates. Emtpy squares show the location of the largest historical earthquakes, taken from the CPTI15 catalogue (Rovida *et al.* 2016).

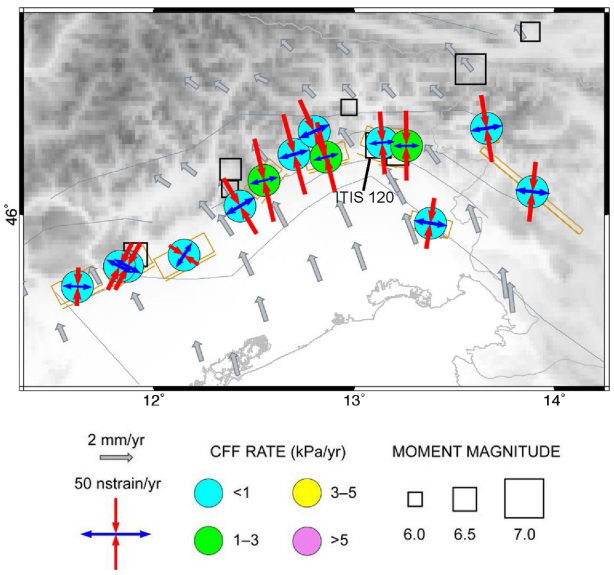

Figure 8. Relation between the principal directions of the geodetic strain rate tensor and the strike of the ISSs. The figure shows that the strike of structures near the tip of the Adriatic indenter, conventionally located at 13.2E, 46.1 N, is nearly orthogonal to the direction of compression.

strikes at 45° to the faults, which is the direction expected for activating strike-slip motion. The 45° offset of the horizontal principal stress axes relative to the fault strike is also well illustrated by the Central Italy strike-slip faults trending E–W and extending between the central Apennine backbone and the coasts of the Adriatic Sea.

In Table 2, we compare the strike of selected seismogenic faults (normal and reverse/trhust) with the direction inferred from the eigenvectors of the strain rate tensor. The Gemona ISS is associated with the 1976 May 6, M_w 6.5 Friuli earthquake; the two Colfiorito ISSs are associated with the 1997 September 26, M_w 5.7 and 6.0 Colfiorito earthquakes; the Paganica ISS with the 2009 April 6, M_w 6.3 L'Aquila earthquake; the Mirandola and Finale Emilia ISSs with the 2012 May 20 and 29, M_w 6.1 and 6.0 earthquakes. As mentioned eralier, for the sake of completeness we also considered the recent 2016 August 24, M_w 6.0 Amatrice and 2016 October 30, M_w 6.5 Norcia earthquakes, though they are not yet listed in DISS. For these earthquakes we assumed the plane dipping to the SW as the actual rupture plane, in agreement with aftershocks distributions and with structural evidence (Chiaraluce *et al.* 2017). Considering that the overall uncertainty in the strike angle is in the order of 20–30°, we conclude that the geologically determined angles are consistent with the directions of maximum strain rate, at least for these seismogenic sources.

Does a large CFF rate necessarily imply a larger probability of activation? If a stress drop of about 3 MPa is taken as reference (Allmann & Shearer 2009), then some 600 yr would be needed to a fault loading at a rate of 5 kPa yr^{-1} to make up the stress which on average is released seismically. This loading time is of the same order of magnitude as the recurrence time inferred from the local Gutenberg–Richter parameters for M_w 6.0–6.5 earthquakes (Wedmore *et al.* 2017). The load on a fault is however determined not only by the regional load discussed in this paper, but also by the stress transferred over the centuries by nearby earthquakes (e.g. King *et al.* 1994). Wedmore *et al.* (2017) have shown that fault interaction in the Central Apennines can significantly affect earthquake recurrence intervals. In perspective, a first approximation to the total load on each fault could be estimated by adding the regional and transferred stresses, using the orientation of the measured stress as a constraint. Hence, the time interval used to integrate the stressing rate could in principle be calibrated by the orientation of the total stress, measured just after the earthquake. This computed stress, however, may still not be a measure of the probability of activation of the fault. We know very little about the ability of each fault to release stress aseismically, nor is it clear if and to what extent these faults can translate the applied stress into permanent deformation. A central question is how we can address systematically the relation between the *a, b* parameters of the regional Gutenberg–Richter law and the loading rates. The regional stress drop is a key parameter to assess the seismicity of an area. Its maximum value is constrained by the geodetic strain rate and by the regional Gutenberg–Richter parameters (Caporali *et al.* 2011). A number of investigators (e.g. Spada *et al.* 2013; Scholz 2015; Chen *et al.* 2016) have recently pointed out that the *b*-value could be related to differences between the maximum and minimum principal stress. These stresses are laterally variable and time dependent, as shown in this paper. Whence the inference that the *b* value could be time dependent, besides being a function of the stress regime and depth, due to the crustal rheology and rock heterogeneity (Mori & Abercrombie 1997).

7.3 Sources with a stress regime different from the geodetically inferred strain rate

Most of the sources with inconsistent stress/stain rate regime did not comply with at least one of the criteria (a), (b) and (c) discussed in Section 4 and were therefore discarded. The only exception is the ITIS140 (Fig. 9), a source associated with 2 January 1117, M_w 6.7, 'Veronese' earhquake, although this assignment is still debated by

Table 2. Analysis of the angle offset between the strike supplied in the DISS database (substituted by the strike from the moment tensor solution for the Amatrice and Norcia earthquakes) and that given by the GNSS strain rate field ('Geodetic strike') for selected seismogenic sources of known fault plane solution, as determined with modern instrumentation (>1976). The uncertainties in the angles are in the order of 20–30°, implying that the differences are in most cases compatible with the overall uncertainty. The formal uncertainty in the geodetic strike is in the order of 8° (see Section 6 for further details).

Lon (°E)	Lat (°N)	ID	Name	Strike (°)	DISS–geodetic strike difference (°)
13.14	46.25	ITIS120	Gemona South	290	25
12.84	43.09	ITIS017	Colfiorito North	143	−3
12.93	43.00	ITIS018	Colfiorito South	148	−1
13.45	42.32	ITIS131	Paganica	133	−11
11.07	44.85	ITIS107	Mirandola	108	33
11.32	44.85	ITIS134	Finale Emilia	115	21.
13.20	*42.75*	*EQ240816*	*Amatrice*	*157*	*11*
13.11	*42.84*	*EQ301016*	*Norcia*	*151*	*−13*

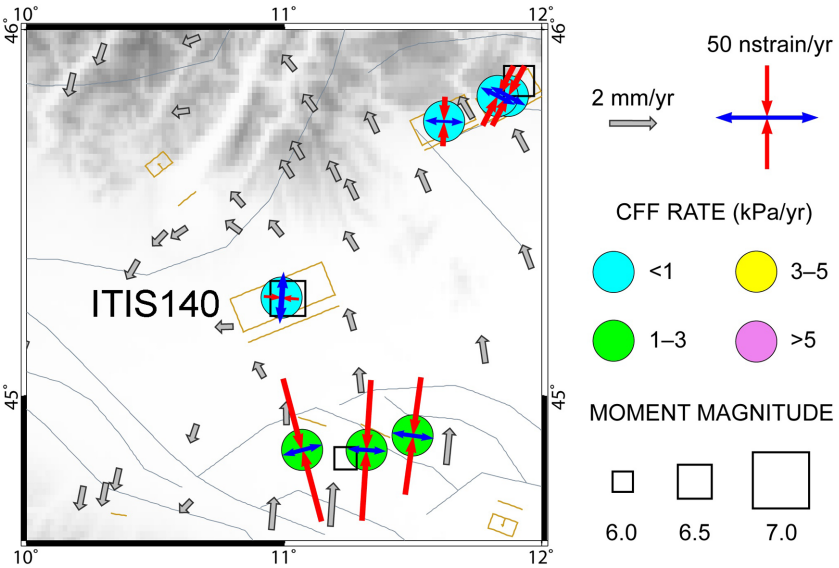

Figure 9. ITIS140 'Veronese' is an example of a seismogenic source that is interpreted as contractional by the compilers of DISS, but that is currently undergoing moderate extension according to the GNSS data.

other investigators (Galadini *et al.* 2005; Galli 2005). The geodetic data point to an extensional regime (Fig. 8), whereas according to DISS, drainage and topographic anomalies are consistent with a buried reverse fault which should represent the reactivation of a former extensional fault. Its CFF rate is negative (Table 1), but the value is within the uncertainty and hence is not significantly different from zero.

8 CONCLUSIONS

The coupling between the regional stress rate field inferred from a large body of GNSS data and the fault geometries described in the DISS database provides important information on the loading/unloading of presumed active Italian seismogenic sources, ultimately supplying confirmation of the state of activity and tectonic style for most of them. Our analysis provides a first quantitative assessment for this regional loading rate. Sources located in northeastern Italy, where the Adria microplate is actively indenting the southern eastern Alps, all appear to be currently loading. We highlight sources for which the loading rate is larger than average, all located in the Apennines. The computed loading rates should be considered preliminary, however, as they rest on a number of critical assumptions: the conversion of scattered GNSS velocities to strain rates and the related interpolation scheme require assumptions on the smoothing filter, which may alter the final estimates of the strain rates, both in magnitude and orientation. We have further assumed nominal values for the Lamé constants, regardless of the seismological constraints on their expected lateral variations. Finally, we do not know pointwise the exact value of the friction coefficient, but we have verified that our basic conclusions do not change significantly if we vary this coefficient across the range 0.2–0.8, based on the relationship between the rake and dip angles of each ISS. Maximum magnitudes and CFF rates appear uncorrelated, however, as shown by the Amatrice/Norcia (2016) and Tocco da Casauria (1456) extensional/transtensional earthquakes, both of magnitude 6.0 or larger, but with quite different CFF rates (Table 1): less than 1 kPa yr^{-1} and larger than 5 kPa yr^{-1}, respectively. Likewise for compressional earthquakes, the Mirandola (ITIS107) and Gemona (ITIS120) earthquakes of 2012 and 1976, both of magnitude 6 or larger, exhibit CFF rates differing by a factor of about 2, as shown in Table 1.

Overall, the qualitative picture implied by the tectonics, geomorphology and contemporary seismicity of the Italian territory is well complemented by our quantitative estimates of loading rates. They confirm the central Apennines as the area where the energy transfer from the regional stress field to a number of known faults is taking

place at the highest rate: tensile stress prevails in such cases. Areas under compressional stress such as Northeast Italy or the Northern Outer Apennines exhibit a somewhat smaller energy transfer rate. Finally, the maximum magnitude of Italian earthquakes seems independent of the intensity of the loading rate.

ACKNOWLEDGEMENTS

The GNSS velocity data used in this paper can be obtained from the corresponding author (alessandro.caporali@unipd.it), or by visiting the web page http://retegnssveneto.cisas.unipd.it/Web/page.php?pid=db&n=15&link=Bollettini_Bernese&chain=10&smo=10 (last accessed on 2018 February 19).

DISS 3.2.0 data are available at http://diss.rm.ingv.it/diss/ (last accessed on 2018 February 19).

This research was supported as an internal project of the institutions involved. We warmly acknowledge the critical and constructive comments of three anonymous referees.

REFERENCES

Allmann, B.P. & Shearer, P.M., 2009. Global variations of stress drop for moderate to large earthquakes, *J. geophys. Res.,* **114**(B1), B01310, doi:10.1029/2008JB005821.

Anderlini, L., Serpelloni, E. & Belardinelli, M.E., 2016. Creep and locking of a low-angle normal fault: insights from the Altotiberina fault in the Northern Apennines (Italy), *Geophys. Res. Lett.,* **43**(9), 4321–4329.

Anderson, E.M., 1951. *The Dynamics of Faulting and Dyke Formation with Applications to Britain*. Oliver and Boyd, Ltd., pp. 206.

Basili, R., Valensise, G., Vannoli, P., Burrato, P., Fracassi, U., Mariano, S., Tiberti, M.M. & Boschi, E., 2008. The Database of Individual Seismogenic Sources (DISS), version 3: summarizing 20 years of research on Italy's earthquake geology, *Tectonophysics,* **453**(1-4), 20–43.

Bressan, G., Ponton, M., Rossi, G. & Urban, S., 2016. Spatial organization of seismicity and fracture pattern in NE Italy and W Slovenia, *J. Seismol.,* **20**(2), 511–534.

Burov, E.B., 2010. The equivalent elastic thickness (Te), seismicity and the long-term rheology of continental lithosphere: time to burn-out "crème brûlée"?: insights from large-scale geodynamic modeling, *Tectonophysics,* **484**(1-4), 4–26.

Caporali, A., 2003. Average strain rate in the Italian crust inferred from a permanent GNSS network–I. Statistical analysis of the time-series of permanent GNSS stations, *Geophys. J. Int.,* **155,** 214–253.

Caporali, A., Barba, S., Carafa, M.M.C., Devoti, R., Pietrantonio, G. & Riguzzi, F., 2011. Static stress drop as determined from geodetic strain rates and statistical seismicity, *J. geophys. Res.,* **116**(B2), B02410, doi: 10.1029/2010JB007671.

Caporali, A., Martin, S. & Massironi, M., 2003. Average strain rate in the Italian crust inferred from a permanent GPS network–II. Strain rate versus seismicity and structural geology, *Geophy. J. Int.,* **155**(1), 254–268.

Caporali, A. *et al.*, 2016. Stress drop at the Kephalonia Transform Zone estimated from the 2014 seismic sequence, *Tectonophysics,* **666,** 164–172.

Carafa, M.M.C. & Barba, S., 2013. The stress field in Europe: optimal orientations with confidence limits, *Geophys. J. Int.,* **193**(2), 531–548.

Carafa, M.M.C., Barba, S. & Bird, P., 2015. Neotectonics and long-term seismicity in Europe and the Mediterranean region, *J. geophys. Res. Solid Earth,* **120**(7), 5311–5342.

Carafa, M.M.C. & Bird, P., 2016. Improving deformation models by discounting transient signals in geodetic data: 2. Geodetic data, stress directions, and long-term strain rates in Italy, *J. geophys. Res. Solid Earth,* **121**(7), 5557–5575.

Carafa, M.M.C., Valensise, G. & Bird, P., 2017. Assessing the seismic coupling of shallow continental faults and its impact on seismic hazard estimates: a case-study from Italy, *Geophys. J. Int.,* **209,** 32–47.

Catalli, F., Cocco, M., Console, R. & Chiaraluce, L., 2008. Modeling seismicity rate changes during the 1997 Umbria-Marche sequence (central Italy) through a rate- and state-dependent model, *J. geophys. Res.,* **113**(B11), B11301, doi:10.1029/2007JB005356.

Chen, Y.L., Hung, S.H., Jiang, J.S. & Chiao, L.Y., 2016. Systematic correlations of the earthquake frequency-magnitude distribution with the deformation and mechanical regimes in the Taiwan orogen, *Geophys. Res. Lett.,* **43**(10), 5017–5025.

Chiarabba, C. & De Gori, P., 2016. The seismogenic thickness in Italy: constraints on potential magnitude and seismic hazard, *Terra Nova,* **28**(6), 402–408.

Chiarabba, C. *et al.*, 2005. Mainshocks and aftershocks of the 2002 Molise seismic sequence, southern Italy, *J. Seismol,* **9**(4), 487–494.

Chiaraluce, L. *et al.*, 2017. The 2016 Central Italy seismic sequence: a first look at the mainshocks, aftershocks, and source models, *Seismol. Res. Lett.,* **88**(3), 757–771.

Console, R., Murru, M., Falcone, G. & Catalli, F., 2008. Stress interaction effect on the occurrence probability of characteristic earthquakes in Central Apennines, *J. geophys. Res.,* **113**(B8), B08313, doi:10.1029/2007JB005418.

Cowie, P.A. *et al.*, 2017. Orogen-scale uplift in the central Italian Apennines drives episodic behaviour of earthquake faults, *Sci. Rep.,* **7,** article number: 44858. doi:10.1038/srep44858.

Dahm, T., Cesca, S., Hainzl, S., Braun, T. & Krüger, F., 2015. Discrimination between induced, triggered, and natural earthquakes close to hydrocarbon reservoirs: a probabilistic approach based on the modeling of depletion-induced stress changes and seismological source parameters, *J. geophys. Res. Solid Earth,* **120**(4), 2491–2509.

Devoti, R., Esposito, A., Pietrantonio, G., Pisani, A.R. & Riguzzi, F., 2011. Evidence of large scale deformation patterns from GPS data in the Italian subduction boundary, *Earth planet. Sci. Lett.,* **311**(3-4), 230–241.

Di Bucci, D. & Mazzoli, S., 2003. The October-November 2002 Molise seismic sequence (southern Italy): an expression of Adria intraplate deformation, *J. geol. Soc.,* **160**(4), 503–506.

Di Luccio, F., Fukuyama, E. & Pino, N.A., 2005. The 2002 Molise earthquake sequence: what can we learn about the tectonics of southern Italy? *Tectonophysics,* **405**(1-4), 141–154.

DISS Working Group, 2015., Database of Individual Seismogenic Sources (DISS), Version 3.2.0: a compilation of potential sources for earth- quakes larger than M 5.5 in Italy and surrounding areas. © INGV 2015 - Istituto Nazionale di Geofisica e Vulcanologia, doi:10.6092/INGV.IT-DISS3.2.0. Available at: http://diss.rm.ingv.it/diss/.

Fracassi, U. & Valensise, G., 2007. Unveiling the sources of the catastrophic 1456 multiple earthquake: hints to an unexplored tectonic mechanism in Southern Italy, *Bull. seismol. Soc. Am.,* **97**(3), 725–748.

Galadini, F., Poli, M.E. & Zanferrari, A., 2005. Seismogenic sources potentially responsible for earthquakes with M C 6 in the eastern Southern Alps (Thiene-Udine sector, NE Italy), *Geophys. J. Int.,* **161**(3), 739–762.

Galli, P., 2005. I terremoti del gennaio 1117. Ipotesi di un epicentro nel cremonese, *Il Quaternario (It. J. Quat. Sci.),* **18**(2), 87–100.

Galli, P., Galadini, F. & Pantosti, D., 2008. Twenty years of paleoseismology in Italy, *Earth Sci. Rev.,* **88**(1-2), 89–117.

Heidbach, O., Reinecker, J., Tingay, M., Mueller, B., Sperner, B., Fuchs, K. & Wenzel, F., 2007. Plate boundary forces are not enough: second and third order stress patterns highlighted in the World Stress Map database, *Tectonics,* **26,** TC6014, doi:10.1029/2007TC002133.

Heidbach, O., Tingay, M., Barth, A., Reinecker, J., Kurfeß, D. & Müller, B., 2010. Global crustal stress pattern based on the World Stress Map database release 2008, *Tectonophysics,* **482**(1-4), 3–15.

King, G. & Cocco, M., 2000. Fault interaction by elastic stress changes: new clues from earthquake sequences, *Adv. Geophys.,* **44,** 1–36.

King, G.C.P., Stein, R.S. & Lin, J., 1994. Static stress changes and the triggering of earthquakes. *Bull. seism. Soc. Am.,* **84**(3), 935–953.

Lin, J. & Stein, R.S., 2004. Stress triggering in thrust and subduction earthquakes and stress interaction between the southern San Andreas and nearby thrust and strike-slip faults, *J. geophys. Res.,* **109**(B2), B02303, doi:10.1029/2003JB002607.

Mariucci, M.T. & Montone, P., 2018. *IPSI 1.1, Database of Italian Present-day Stress Indicators,* Istituto Nazionale di Geofisica e Vulcanologia (INGV). doi:http://doi.org/10.6092/INGV.IT-IPSI.1.1.

Massironi, M., Zampieri, D. & Caporali, A., 2006. Miocene to present major fault linkages through the Adriatic indenter and the Austroalpine-Penninic collisional wedge (Alps of NE Italy), *Geol. Soc. London Spec. Pub.,* **262**(1), 245–258.

Mastrolembo Ventura, B. & Caporali, A., 2017. Stress and strain rate fields: a comparative analysis for the Italian territory, *Boll. Geofis. Teor. Appl.,* **58**(3), 265–284.

Meade, B.J., DeVries, P.M.R., Faller, J., Viegas, F. & Wattenberg, M., 2017. What's better than Coulomb failure stress? A ranking of scalar static stress triggering mechanisms from 105 mainshock-aftershock pairs, *J. geophys. Res. Solid Earth,* **44,** 11,409–11,416.

Meletti, C., Patacca, E. & Scandone, P., 2000. Construction of a seismotectonic model: the case of Italy, *Pure appl. geophys.,* **157**(1), 11–35.

Michelini, A. & Bolt, B.A., 1986. Application of the principal parameter method to the 1983 Coalinga, California aftershock sequence, *Bull. seism. Soc. Am.,* **76,** 409–420.

Montone, P. & Mariucci, M.T., 2016. The new release of the Italian contemporary stress map, *Geophys. J. Int.,* **205**(3), 1525–1531.

Montone, P., Mariucci, M.T. & Pierdominici, S., 2012. The Italian present-day stress map, *Geophys. J. Int.,* **189**(2), 705–716.

Moreno, M., Rosenau, M. & Oncken, O., 2010. 2010 Maule earthquake slip correlates with pre-seismic locking of Andean subduction zone, *Nature,* **467**(7312), 198–202.

Mori, J. & Abercrombie, R.E., 1997. Depth dependence of earthquake frequency-magnitude distributions in California: implications for rupture initiation, *J. geophys. Res.,* **102**(B7), 15081–15090.

Nalbant, S.S., McCloskey, J., Steacy, S. & Barka, A.A., 2002. Stress accumulation and increased seismic risk in eastern Turkey, *Earth planet. Sci. Lett.,* **195**(3-4), 291–298.

Palano, M., 2015. On the present-day crustal stress, strain-rate fields and mantle anisotropy pattern of Italy, *Geophys. J. Int.,* **200**(2), 969–985.

Pierdominici, S. & Heidbach, O., 2012. Stress field of Italy – mean stress orientation at different depths and wave-length of the stress pattern, *Tectonophysics,* **532,** 301–311.

Restivo, A., Bressan, G. & Sugan, M., 2016. Stress and strain patterns in the Venetian Prealps (north-eastern Italy) based on focal-mechanism solutions, *Boll. Geofis. Teor. Appl.,* **57**(1), 13–30.

Rivera, L. & Kanamori, H., 2002. Spatial heterogeneity of tectonic stress and friction in the crust, *Geophys. Res. Lett.,* **29**(6), doi:10.1029/2001GL013803.

Robl, J., Heberer, B., Prasicek, G., Neubauer, F. & Hergarten, S., 2017. The topography of a continental indenter: the interplay between crustal deformation, erosion, and base level changes in the eastern Southern Alps, *J. geophys. Res. Earth Surf.,* **122**(1), 310–334.

Rovida, A., Locati, M., Camassi, R., Lolli, B. & Gasperini, P., Eds, 2016, CPTI15, the 2015 version of the parametric catalogue of Italian earthquakes, Istituto Nazionale di Geofisica e Vulcanologia, doi:http://doi.org/10.6092/INGV.IT-CPTI15.

Scholz, C.H., 2015. On the stress dependence of the earthquake b value, *Geophys. Res. Lett.,* **42**(5), 1399–1402.

Smith, S.A.F. & Faulkner, D.R., 2010. Laboratory measurements of the frictional properties of the Zuccale low-angle normal fault, Elba Island, Italy, *J. geophys. Res.,* **115**(B2), B02407, doi:10.1029/2008JB006274.

Spada, M., Tormann, T., Wiemer, S. & Enescu, B., 2013. Generic dependence of the frequency-size distribution of earthquakes on depth and its relation to the strength profile of the crust, *Geophys. Res. Lett.,* **40**(4), 709–714.

Stein, R.S., Barka, A.A. & Dietrich, J.H., 1997. Progressive failure on the North Anatolian fault since 1939 by earthquake stress triggering, *Geophys. J. Int.,* **128**(3), 594–604.

Toda, S., Stein, R.S., Richards-Dinger, K. & Bozkurt, S., 2005. Forecasting the evolution of seismicity in southern California: animations built on earthquake stress transfer, *J. geophys. Res.,* **110**(B5), B05S16, doi:10.1029/2004JB003415.

Turcotte, D.L. & Schubert, G., 2014. *Geodynamics,* 3rd edn, Cambridge Univ. Press, pp, 623.

Valensise, G. & Pantosti, D., 2001. The investigation of potential earthquake sources in peninsular Italy: a review, *J. Seismol.,* **5**(3), 287–306.

Valensise, G., Pantosti, D. & Basili, R., 2004. Seismology and tectonic setting of the 2002 Molise, Italy, earthquake, *Earthquake Spectra,* **20**(S1), S23–S37.

Vallée, M. & Di Luccio, F., 2005. Source analysis of the 2002 Molise, southern Italy, twin earthquakes (10/31 and 11/01), *Geophys. Res. Lett.,* **32**(12), L12309.

Valoroso, L., Chiaraluce, L., Piccinini, D., Di Stefano, R., Schaff, D. & Waldhauser, F., 2013. Radiography of a normal fault system by 64,000 high-precision earthquake locations: the 2009 L'Aquila (central Italy) case study, *J. geophys. Res.,* **118,** 1,156–1,176.

Viganò, A., Scafidi, D., Martin, S. & Spallarossa, D., 2013. Structure and properties of the Adriatic crust in the central-eastern Southern Alps (Italy) from local earthquake tomography, *Terra Nova,* **25**(6), 504–512.

Viganò, A., Scafidi, D., Ranalli, G., Martin, S., Della Vedova, B. & Spallarossa, D., 2015. Earthquake relocations, crustal rheology, and active deformation in the central-eastern Alps (N Italy), *Tectonophysics,* **661,** 81–98.

Wedmore, L.N.J., Faure Walker, J.P., Roberts, G.P., Sammonds, P.R., McCaffrey, K.J.W. & Cowie, P.A., 2017. A 667 year record of coseismic and interseismic Coulomb stress changes in central Italy reveals the role of fault interaction in controlling irregular earthquake recurrence intervals, *J. geophys. Res. Solid Earth,* **122**(7), 5691–5711.

Wu, Y., Jiang, Z., Yang, G., Wei, W. & Liu, X., 2011. Comparison of GPS strain rate computing methods and their reliability, *Geophys. J. Int.,* **185**(2), 703–717.

SUPPORTING INFORMATION

Supplementary data are available at *GJI* online.
AdditionalMaterialGJIrev1TAR.zip.
Please note: Oxford University Press is not responsible for the content or functionality of any supporting materials supplied by the authors. Any queries (other than missing material) should be directed to the corresponding author for the paper.

APPENDIX A

1. Least squares collocation as a minimum variance algorithm for interpolation

Let v_i $(i = 1...n)$ be the value of the velocity v (either east or north component) sampled at n points. The expectation value of v at a point P is represented as a linear combination of the data points v_i with unknown coefficients a_{Pi}:

$$\hat{v}_P = \mathrm{E}\,(v_P|v_1, \ldots, v_n) = \sum_{i=1}^{n} a_{Pi} v_i + \epsilon_P$$

where v_P is the true but unknown value of v at P and ϵ_P is the model error. We compute the coefficients a_{Pi} by minimizing the error variance $|v_P - \hat{v}_P|^2$.

To this purpose the variance is expanded as follows:

$$\epsilon_P^2 = \hat{v}_P^2 - 2\hat{v}_P \sum_{i=1}^{n} a_{Pi} v_i + \sum_{i,j=1}^{n} a_{Pi} v_i a_{Pj} v_j$$

A necessary condition for minimal variance on the coefficients a_{pi} is that

$$\frac{\partial \epsilon_P^2}{\partial a_{Pk}} = -2\hat{v}_P v_k + 2 \sum\nolimits_{i=1}^{n} a_{Pi} v_i v_k = 0 \qquad (10)$$

We introduce the correlation function of the velocity:

$$C_{Pi} = \langle \hat{v}_P v_i \rangle;\ C_{ij} = \langle v_i v_j \rangle$$

Eq. (A1) can be formally solved:

$$a_{Pi} = \sum_{j=1}^{n} C_{Pj} C_{ji}^{-1}.$$

2. Explicit form of the correlation function and computation of the strain rate

The correlation function is often approximated by a harmonic function falling off as the inverse squared of the distance and with zero derivative at the origin (E and N denote UTM east and north coordinates):

$$C_{Pi} = \frac{1}{1 + \left(\frac{d_{Pi}}{d_0}\right)^2}; \; d_{Pi} = \sqrt{(\mathrm{E}_P - \mathrm{E}_i)^2 + (\mathrm{N}_P - \mathrm{N}_i)^2}.$$

The scale distance d_0 is determined by the velocity data themselves or – as done in this paper – by the behaviour of the shear strain rate. Normally, one correlation function is assumed for both the east and north component of the velocity.

At point P the velocity is then:

$$\hat{v}_P = \sum_{j=1}^{n} C_{pj} C_{ji}^{-1} \, v_j$$

and its horizontal gradient in the E direction of east or north component of the velocity interpolated at P is

$$\frac{\partial \hat{v}_P}{\partial \mathrm{E}_P} = \sum_{j=1}^{n} \frac{\partial C_{Pj}}{\partial \mathrm{E}_P} C_{ji}^{-1} \, v_j$$

with

$$\frac{\partial C_{Pj}}{\partial \mathrm{E}_P} = -2\left(C_{Pj}\right)^2 \frac{\mathrm{E}_P - \mathrm{E}_j}{d_0^2}.$$

Likewise for the horizontal gradient in the north direction.

APPENDIX B

1. Normal **n** and tangential **d** versors to the fault plane as a function of strike α , dip δ and rake λ (1, 2, and 3 denote east, north and up components, respectively)

$$d_1 = \cos\lambda\sin\alpha - \cos\delta\sin\lambda\cos\alpha$$

$$d_2 = \cos\lambda\cos\alpha + \cos\delta\sin\lambda\sin\alpha$$

$$d_3 = \sin\delta\sin\lambda$$

$$n_1 = \sin\delta\cos\alpha$$

$$n_2 = -\sin\delta\sin\alpha$$

$$n_3 = \cos\delta.$$

2. Tangential stress

$$\begin{aligned}\tau \; = \; & \sigma_{11}\left(-\sin\lambda\cos^2\alpha\,\tfrac{\sin 2\delta}{2} + \cos\lambda\,\sin\delta\,\tfrac{\sin 2\alpha}{2}\right)\\ & +\sigma_{12}\left(\sin\lambda\,\sin 2\alpha\,\tfrac{\sin 2\delta}{2} + \cos\lambda\,\sin\delta\,\cos 2\alpha\right)\\ & +\sigma_{13}\left(-\sin\lambda\,\cos\alpha\,\cos 2\delta + \cos\lambda\,\sin\alpha\,\cos\delta\right)\\ & +\sigma_{23}\left(\sin\lambda\,\sin\alpha\,\cos 2\delta + \cos\lambda\,\cos\alpha\,\cos\delta\right)\\ & +\sigma_{22}\left(-\sin\lambda\,\tfrac{\sin 2\delta}{2}\sin^2\alpha - \cos\lambda\,\tfrac{\sin 2\alpha}{2}\,\sin\delta\right) + \sigma_{33}\left(\sin\lambda\,\tfrac{\sin 2\delta}{2}\right).\end{aligned}$$

3. Normal stress

$$\begin{aligned}\sigma_n \; = \; & \sigma_{11}\,\sin^2\delta\cos^2\alpha + \sigma_{22}\sin^2\delta\sin^2\alpha + \sigma_{33}\cos^2\delta\\ & -\sigma_{12}\sin^2\delta\,\sin 2\alpha + \sigma_{13}\cos\alpha\,\sin 2\delta - \sigma_{23}\sin\alpha\,\sin 2\delta.\end{aligned}$$

4. Coulomb failure function

$$\begin{aligned}\mathrm{CFF} = \; & \left(\mu_f \sin^2\delta - \sin\lambda\,\tfrac{\sin 2\delta}{2}\right)\left[\sigma_{11}\cos^2\alpha - \sigma_{12}\,\sin 2\alpha + \sigma_{22}\sin^2\alpha\right]\\ & +\cos\lambda\,\sin\delta\left[(\sigma_{11} - \sigma_{22})\,\tfrac{\sin 2\alpha}{2} + \sigma_{12}\cos 2\alpha\right]\\ & +(\mu_f\sin 2\delta - \sin\lambda\cos 2\delta)(\sigma_{23}\sin\alpha - \sigma_{13}\cos\alpha)\\ & +\cos\lambda\cos\delta\,(\sigma_{23}\cos\alpha - \sigma_{13}\sin\alpha)\\ & +\sigma_{33}\left(\sin\lambda\,\tfrac{\sin 2\delta}{2} - \mu_f\cos^2\delta\right).\end{aligned}$$

5. Derivative of CFF w.r.t. dip for 2D stress ($\sigma_{i3} = 0$, $i = 1,3$)

$$\begin{aligned}\frac{\partial \mathrm{CFF}}{\partial\delta} = \; & (\mu_f\sin 2\delta - \sin\lambda\,\cos 2\delta)\\ & \times\left[\sigma_{11}\,\cos^2\alpha - \sigma_{12}\,\sin 2\alpha + \sigma_{22}\,\sin^2\alpha\right]\\ & +\cos\lambda\,\cos\delta\left[(\sigma_{11} - \sigma_{22})\,\frac{\sin 2\alpha}{2} + \sigma_{12}\cos 2\alpha\right].\end{aligned}$$

We note that if the strike α of the fault, as given in the DISS, defines a principal direction of the stress rate tensor, then the first squared parenthesis is the normal stress and the second squared parenthesis is zero. Imposing that the derivative is zero yields the familiar relation between friction and the dip and rake angles. The derivative of the CFF relative to rake poses no constraints on the friction.

Taking the derivative of the CFF relative to strike and rake we conclude that a necessary condition for the CFF to be maximum in the plane stress case is that:

$$\tan 2\alpha \; = \frac{2\sigma_{12}}{(\sigma_{22} - \sigma_{11})}$$

$$\tan 2\delta \; = \frac{\sin\lambda}{\mu_f}$$

$$\lambda \; = \; \pm 90.$$

Thus, the fault must be aligned with the principal axis of the stress tensor (first equation), the dip, rake and friction must be related with each other (second equation), and the fault must be normal or reverse (third equation).